

## Appearance of metastable B2 phase during solidification of Ni<sub>50</sub>Zr<sub>50</sub> alloy: electrostatic levitation and molecular dynamics simulation studies

This content has been downloaded from IOPscience. Please scroll down to see the full text.

[View the table of contents for this issue](#), or go to the [journal homepage](#) for more

Download details:

IP Address: 129.186.252.219

This content was downloaded on 13/04/2015 at 20:28

Please note that [terms and conditions apply](#).

# Appearance of metastable B2 phase during solidification of Ni<sub>50</sub>Zr<sub>50</sub> alloy: electrostatic levitation and molecular dynamics simulation studies

D G Quirinale<sup>1,2</sup>, G E Rustan<sup>1</sup>, S R Wilson<sup>1</sup>, M J Kramer<sup>1</sup>, A I Goldman<sup>1,2</sup> and M I Mendelev<sup>1</sup>

<sup>1</sup> Division of Materials Sciences and Engineering, Ames Laboratory, Ames, IA 50011, USA

<sup>2</sup> Department of Physics and Astronomy, Iowa State University, Ames, IA 50011, USA

E-mail: [mendelev@ameslab.gov](mailto:mendelev@ameslab.gov)

Received 20 October 2014, revised 21 December 2014

Accepted for publication 8 January 2015

Published 4 February 2015



## Abstract

High-energy x-ray diffraction measurements of undercooled, electrostatically levitated Ni<sub>50</sub>Zr<sub>50</sub> liquid droplets were performed. The observed solidification pathway proceeded through the nucleation and growth of the metastable B2 phase, which persisted for several seconds before the rapid appearance of the stable B33 phase. This sequence is shown to be consistent with predictions from classical nucleation theory using data obtained from molecular dynamics (MD) simulations. A plausible mechanism for the B2–B33 transformation is proposed and investigated through further MD simulations.

Keywords: solidification, x-ray diffraction, molecular dynamics simulation

(Some figures may appear in colour only in the online journal)

## 1. Introduction

In deeply undercooled liquids, metastable solid phases can often influence or dominate the nucleation process, to the extent that metastable phase diagrams have been proposed on the basis of experimental results [1]. The influence of metastable phases is particularly well-documented for pure face-centered cubic (fcc) metals in which the body-centered cubic (bcc) structure is metastable; several experimental [1–4], computational [5, 6] and theoretical [7, 8] studies have shown that the bcc phase can nucleate first and then transform into the equilibrium fcc structure. This phenomenon is in accordance with the phase-selection principle proposed by Stranski and Totomanow [9], who suggested that the phase that appears first has the lowest nucleation barrier, and is not necessarily either the thermodynamically stable phase or the most energetically favorable phase for a given undercooling. The metastable phase may only be present in the system for a very short time, yet its brief existence can define the crystallization mechanism

and rate. Therefore our ability to detect or predict the appearance of this phase is key to describing the solidification process.

Here, we report on high-energy x-ray diffraction measurements of electrostatically levitated 50–50 Ni–Zr liquid droplets in which we observed that the metastable B2 phase nucleated and persisted for several seconds before the appearance of the stable B33 phase. Subsequent molecular dynamics (MD) simulations revealed that the stable B33 phase must overcome a significantly higher nucleation barrier to crystallize from the liquid as compared to the metastable B2 phase, confirming that the Stranski–Totomanow principle holds for more complex crystal structures. Furthermore, MD simulations suggest that the barrier for B2 to B33 transformation is low under conditions which are realized toward the end of the solidification process. Thus, our work suggests that metastable B2 serves as a critical intermediate step in the liquid–B33 transition in Ni<sub>50</sub>Zr<sub>50</sub> that permits the solidification process to bypass what might otherwise be a formidable nucleation barrier.

## 2. Experimental procedure

In order to study solidification in  $\text{Ni}_{50}\text{Zr}_{50}$ , samples of Ni–Zr were electrostatically levitated at the 6ID-D beam line at the Advanced Photon Source at Argonne National Laboratory, permitting *in situ* high-energy x-ray diffraction measurements using x-rays of wavelength 0.09403 Å (131 keV) and a beam size of 0.2 mm × 0.2 mm. The diffraction patterns were recorded on a two-dimensional GE Revolution 41-RT flat panel detector. The samples, spheres of approximately 2.0 to 2.5 mm in diameter, were processed in the Washington University Beamline Electrostatic Levitation furnace as described elsewhere [10]. The sample-to-detector distance as well as the vertical and horizontal tilts of the detector were calibrated using the diffraction from a levitated silicon sphere. The vacuum in the chamber was maintained in the low  $10^{-6}$  Torr range to minimize oxidation during the measurement. Samples were heated using a fiber-coupled diode laser operating at 980 nm, up to 50 W, and the sample temperature was measured by a Process Sensors Metis MQ22 two-color ratio pyrometer utilizing 1.4 and 1.65  $\mu\text{m}$  wavelengths; this helped to correct for any emissivity changes the sample may have undergone throughout processing.

Prior to levitation, the sample was heated close to the melting point several times on the molybdenum launch post to assist in outgassing prior to processing. Once floating and heated through the melt plateau, the sample was heated up to  $\sim 200$  K above the liquidus, the laser was then switched off, and the sample was allowed to free-cool as frames were recorded at a rate of 10 Hz in an attempt to resolve transitory events (see figure 1). The resulting temperature data were later calibrated by matching the measured temperature of the melt plateau to literature values, and then interpolated to match each x-ray frame, assuming no substantial change in emissivity over the measured temperature range. The diffraction patterns were corrected for bad pixels via a pixel intensity map, and dark current subtraction corrections were applied prior to processing. The measured crystalline diffraction patterns were analyzed using GSAS [11] and the Washington University x-ray analysis LabView package [12] as then used to obtain liquid structure factors to correlate with MD simulation results.

Figure 1 shows data taken during one free-cool cycle from a starting temperature of 1773 K, approximately 200 K above the melting plateau. Figure 1(a) shows the correlation observed between the sample temperature and the recorded diffraction pattern as a function of scattering angle as the system evolved over time. Examination of the obtained data clearly shows that the liquid attains a maximum undercooling of approximately 200 K before recrystallizing into the B2 phase and then, a few seconds later, transforming into the B33 phase (figure 1(b)). There is a spike in the thermal data which appears to coincide with the initial appearance of B33, and is consistently observed in all runs; however, it is uncertain whether this spike represents the signature of an actual physical process, or is simply an artifact of the measurement technique and subsequent analysis. The shoulder preceding this spike may be attributed to the latent heat associated with the liquid–B2 transformation, whereas the shoulder following this peak

indicates that a latent heat is likewise associated with the B2–B33 transformation.

## 3. MD simulation

In order to better understand the observed transformation pathway, we turned to MD simulations, which allowed us to compute all parameters required by classical nucleation theory (CNT) [13]. Since *ab initio* MD simulation cannot be used for these calculations [14], we performed classical MD simulations utilizing a semi-empirical potential recently developed for Ni–Zr alloys [15]. This potential provides that B33 is the most stable solid phase from 0 to  $T_m$ , and that B2 is metastable in accordance with experiment. The relative stability of B33 over B2 was accomplished during potential development by including a procedure to fit the B2 melting temperature such that B2 melts roughly 100 K below the B33 solid–liquid transition. It was shown in [15] that when a liquid  $\text{Ni}_{50}\text{Zr}_{50}$  alloy model is created using this potential and seeded with either B2 or B33, the crystal phase is observed to readily grow with the appropriate structure. The good fit reported to the experimental liquid structure, as well as the relative B2/B33 stability, ensures that this potential is suitable for studying solid–liquid transitions in the Ni–Zr system.

Application of standard CNT requires determination of both the bulk driving force for nucleation and the solid–liquid interface (SLI) free energy,  $\gamma(\mathbf{n})$ . The first quantity is determined from the difference in the bulk free energies of liquid and solid phases,  $f\!l.G_m$ , which can be computed via the Gibbs–Helmholtz equation once the melting temperature and the latent heat are obtained from MD simulation (e.g., see [16]). SLI free energies are much more difficult to determine, but a computational method to do so using MD simulation has been developed in [17] and validated in [18]. The B33 measurement listed for reference in table 1 has been reported in detail elsewhere [15]. The method followed for the B2 measurement reported here differs from the method used for the previous B33 computation primarily in that  $\gamma(\mathbf{n})$  has been expanded in this work in terms of the cubic harmonics rather than the orthorhombic harmonics required for B33. Expansion coefficients determined in this way are listed in table 1, and the inclination dependence of the SLI free energy is visualized for both cases in figure 2. Two features are evident from these measurements. First, the value of  $\gamma(\mathbf{n})$  averaged over inclination  $\mathbf{n}$  is roughly 2.5 times larger for B33 than for B2. Second, no inclination is observed for which the value of  $\gamma_{\text{B}2}$  exceeds that of  $\gamma_{\text{B}33}$ . Hence, our MD simulations suggest that it takes substantially more work to create a B33–liquid interface than a B2–liquid interface.

The SLI free energies presented in figure 2 were determined at the melting temperature of each crystal phase. In order to estimate the variation of  $\gamma$  with temperature from these measurements, we followed Aga *et al* [19] and assumed that the empirical Turnbull relation [20] holds in the deeply undercooled state, in which case we may write

$$\gamma_0(T) = C_T \rho^{2/3}(T) f\!l.H_m(T), \quad (1)$$

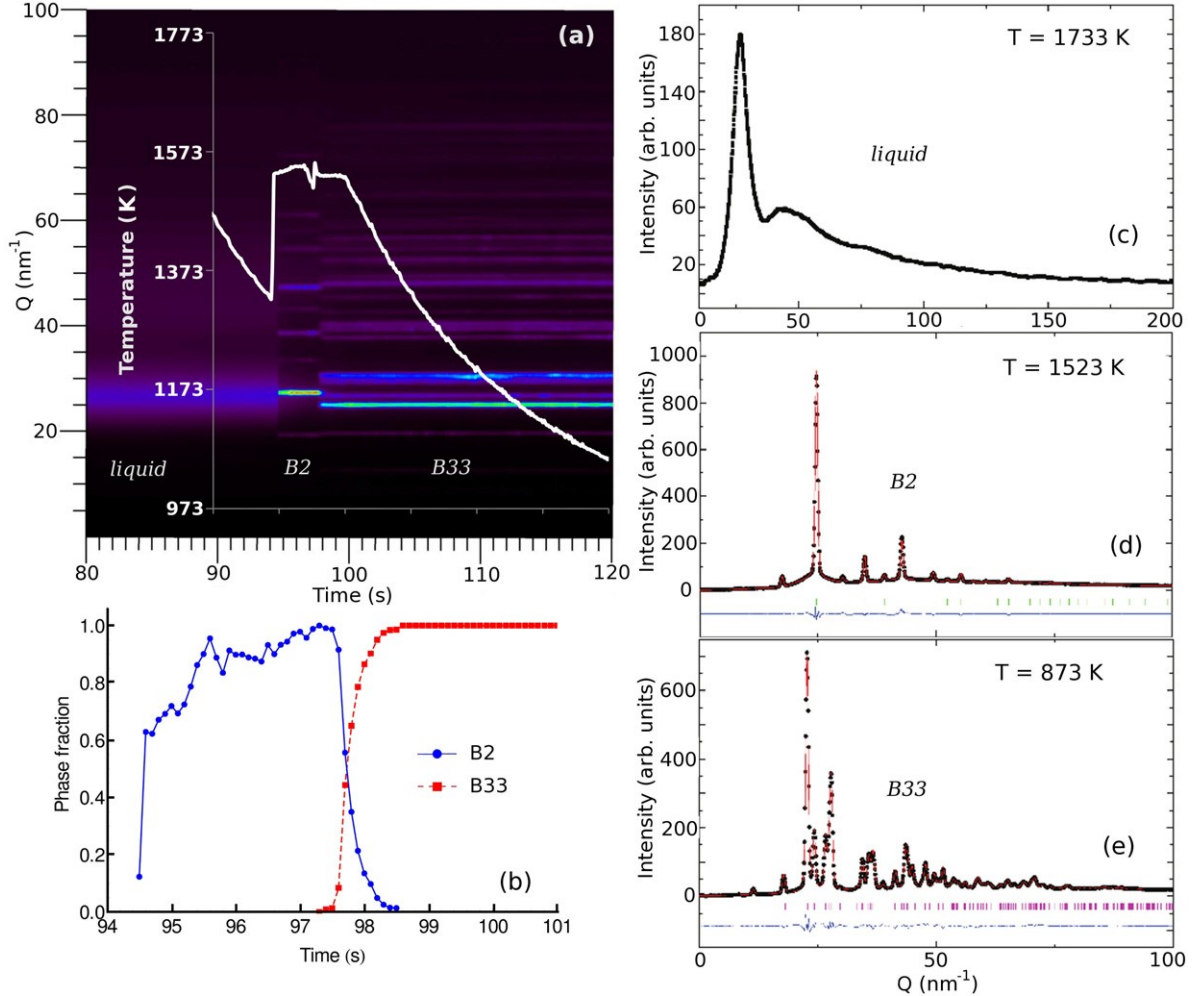


**Figure 1.** The temperature evolution of the x-ray diffraction patterns. (a) shows the sample temperature (white line) measured through one full free-cooling cycle, superimposed over the sequence of x-ray diffraction patterns recorded during this time. The thermal events starting at  $\sim 95$  s correspond to the recalescence from the undercooled liquid to the B2 structure, followed by the B2–B33 transition. (b) shows the phase fraction as a function of time. (c), (d) and (e) show the diffraction patterns taken at 1733 K in the liquid phase, 1523 K in the B2 phase and 873 K in the B33 phase, respectively, along with the fits and residuals from the GSAS refinement. The green tick marks represent the Bragg peak positions associated with the B2 phase and the magenta tick marks describe the B33 Bragg peak positions.

**Table 1.** Coefficients of the appropriate symmetry-adapted spherical harmonic expansion of the SLI free energy, for both the B2 and B33 phases, as determined by MD simulation. The B2 coefficients were determined in the present work, and follow the form of the first-order cubic harmonic expansion introduced in [24]. The B33 coefficients were first reported in [15] and are listed here alongside B2 for comparison. Note that the B33 coefficients represent a second-order expansion in terms of the orthorhombic spherical harmonics.

$\gamma_{B2}$ (mJ m $^{-2}$ )	$\varepsilon_1$	$\varepsilon_2$				
$128 \pm 1$	$-0.009 \pm 0.004$	$0.0008 \pm 0.0006$				
$\gamma_{B33}$ (mJ m $^{-2}$ )	$\varepsilon_{20}$	$\varepsilon_{22}$	$\varepsilon_{40}$	$0.003 \pm 0.006$	$\varepsilon_{42}$	$-\varepsilon_{44} \pm 0.004$
$346 \pm 57$	$0.028 \pm 0.005$	$0.053 \pm 0.008$				$0.002 \pm 0.005$

where  $\rho$  is the solid density,  $f\!l.H_m$  is the enthalpy difference between bulk liquid and solid phases,  $\gamma_0$  is the value of  $\gamma(\mathbf{n})$  averaged over all inclinations, and  $C_T$  is the Turnbull coefficient. The Turnbull coefficient varies only with crystal structure and is therefore expected to remain independent of temperature. With knowledge of  $\rho(T)$ ,  $\gamma_0(T)$  and  $f\!l.G_m(T)$ , standard CNT approximations provide an estimate for the magnitude of the nucleation barrier  $f\!l.G^*$  given by [21]

$$f\!l.G^* = \frac{16\pi}{3} \frac{\gamma_0^3}{\rho^2 f\!l.G_m^2}. \quad (2)$$

Nucleation barriers  $f\!l.G^*$  determined in this way for both B2 and B33 phases are plotted as functions of temperature in figure 2(c). From this figure it can be seen that for all temperatures approximately 100 K below the B2 melting temperature, the B2 nucleation barrier is always less than that for B33. Hence, our MD simulations suggest that the undercooled liquid is significantly more stable with respect to B33 than B2 for undercoolings comparable to the experimentally observed values. Furthermore, figure 2 shows that in experiment crystallization starts approximately 200 K below the B2 melting temperature. The MD data suggest that

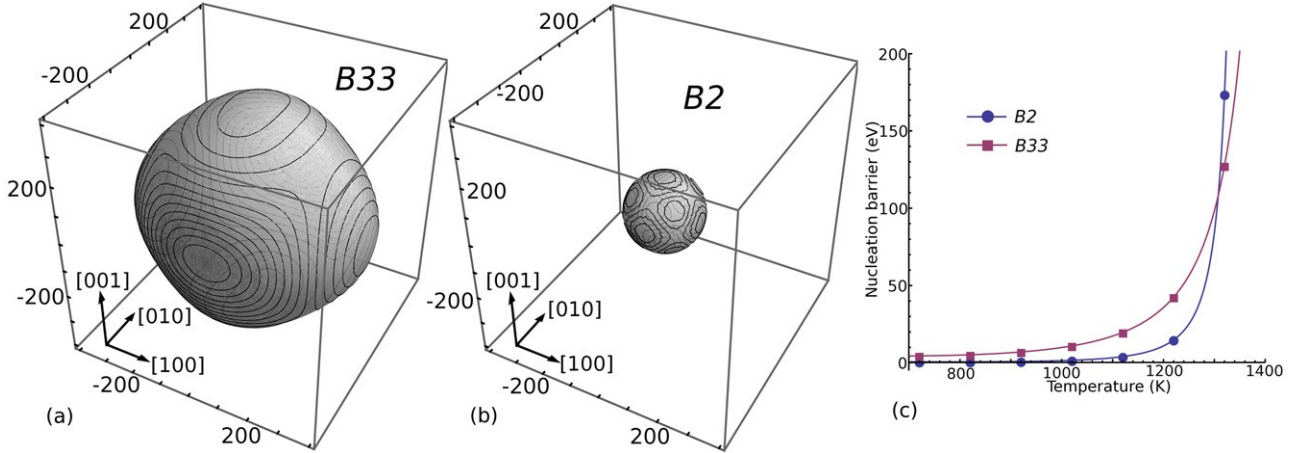


**Figure 2.** (a) and (b) show SLI free energies  $\gamma(\mathbf{n})$  of the B33 and B2 phases, measured at their melting points (1473 K and 1369 K, respectively) from MD simulations, and plotted in 3D as a function of the interface inclination  $\mathbf{n}$  in the crystal reference frame. All values in (a) and (b) are given in units of  $\text{mJ m}^{-2}$ . The value obtained by averaging over all inclinations is  $\gamma_0 = 345.9 \text{ mJ m}^{-2}$  for B33 and  $\gamma_0 = 133.6 \text{ mJ m}^{-2}$  for B2. In (c), the nucleation barrier  $f\Gamma G^*$  for each phase is plotted as a function of temperature using equation (2). The nucleation barrier diverges at the melting point of each phase.

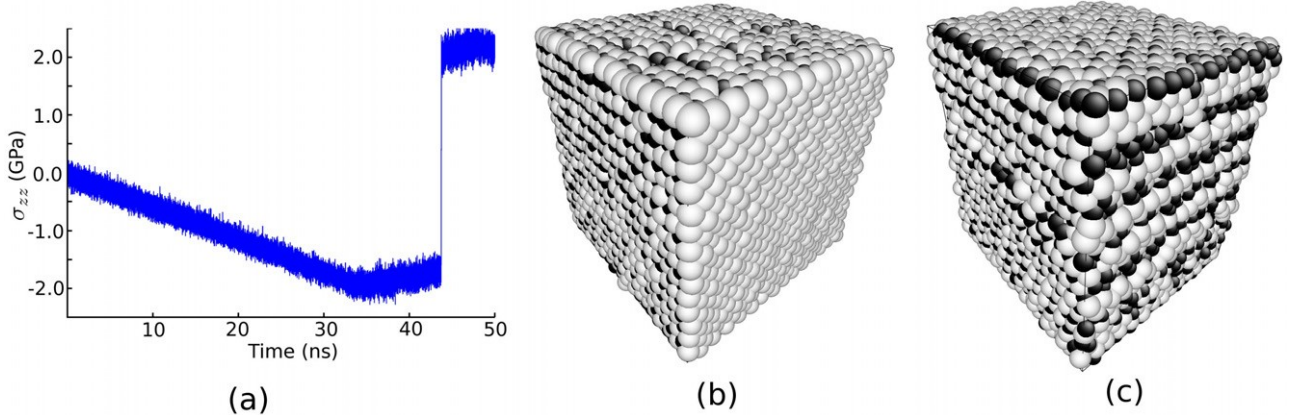


**Figure 3.** Displacive B2 to B33 transformation observed in MD simulation when bulk B2 is subject to tensile stress along the [1 1 0] axis. (b) shows the initial B2 model, whereas (c) is the model at the end of the run. The displacive transformation occurred during the abrupt discontinuity around 44 ns.

at this undercooling the nucleation barrier for B2 is 2.5 times smaller than that for B33. Thus, our MD results are able to explain the appearance of B2 prior to B33 observed in the experiment within the context of standard CNT.

This still leaves open the question of how the B33 phase appears in the alloy. Unfortunately, we cannot use CNT as above to describe this process. Although we can easily determine the bulk driving force for the B2–B33 transformation using the same method as above, we cannot use the capillarity fluctuation method proposed in [17] to determine the B2–B33 interface free energy because there is no equilibrium temperature at which B2 and B33 coexist (B33 is always more stable than B2). Moreover, the solidified droplet probably contains many grain boundaries, so there is no reason to assume that the B33 phase appears as a result of a homogeneous nucleation. Nevertheless, MD simulation allows us to propose a possible scenario for the B2–B33 transformation. We begin with our experimental observations. The phase fractions were determined using Rietveld refinement of the whole pattern. The uncertainty of the volume fraction

was  $\sim 2\%$ . Figure 1(b) shows the relative fractions of B2 and B33 as functions of time. From this data, it can be seen that the B33 transformation is initiated once the B2 transformation is almost complete. Furthermore, although the B2–B33 transformation proceeds much more rapidly than the liquid–B2 transformation, our x-ray diffraction measurements are nonetheless able to resolve the process in time, and the observed rate is orders of magnitude slower than the speed of sound in Ni–Zr. These observations suggest that the B2–B33 transformation involves a nucleation process at select points throughout the sample, associated with the final stages of the liquid–B2 transformation, followed by rapid growth.

Near the end of the solidification of the liquid alloy into B2, it is likely that there are pockets of residual liquid which are completely surrounded by the solid phase. If so, then the pressure inside these liquid droplets should not only be negative but very large because the B2 phase is denser than the liquid phase. Displacive B2–B33 transitions have previously been studied in similar materials, such as (for instance) Ni–Ti [22] and Zr–Co [23] alloys. To test whether this tensile stress

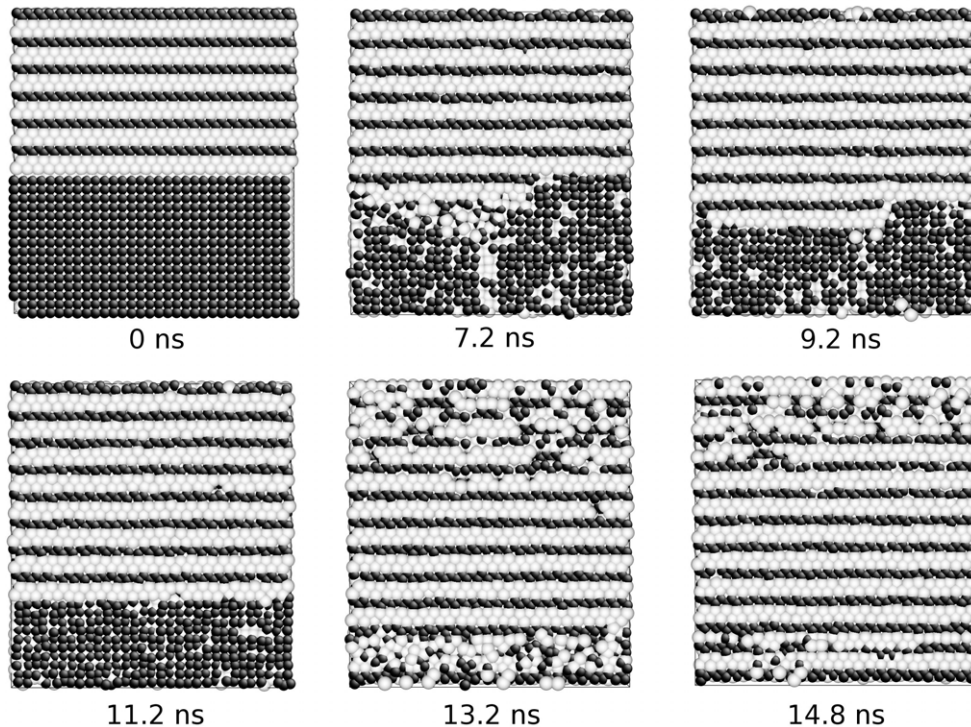


**Figure 4.** Snapshots showing an MD simulation of the evolution of a B2/B33 interface. Each image shows a cross-section of a cube of edge length  $\sim 100$  Å. The full domain contains nearly 66 000 atoms and is evolved in the NPT ensemble under periodic boundary conditions.

can trigger a displacive B2–B33 transformation in Ni–Zr we performed MD simulations in which bulk B2 (approximated as roughly 15 000 atoms under periodic boundary conditions) was subject to uniaxial tension at a constant strain rate of  $1.7 \times 10^6$  s $^{-1}$  along the [1 1 0] axis. Under these loading conditions we observed a displacive transition to B33 when pressures approached  $-2.0$  GPa (figure 3). The resulting B33 [0 1 0] axis was aligned with the original [1 1 0] B2 axis.

The B2–B33 transformation observed experimentally cannot be purely displacive in nature, because the solidified B2 is not under any applied stress. These simulations should instead be understood as predicting the response to any large local stresses that may develop during B2 solidification. Note that the threshold pressure of the displacive B2–B33 transformation obtained above using the potential from [15] is only a rough estimate of its true value since this potential was never fit to describe such a transformation.

If local stresses initiate the B2–B33 transformation, the remaining untransformed material must transform through growth from an initial set of nuclei. Although this transformation is energetically favorable, the rate at which it can occur is limited by the kinetics of B2/B33 interface motion, as dictated by the interface mobility. To determine whether the B2/B33 interface mobility is consistent with the observed B2–B33 transformation rate, we performed further MD simulations at the B2 melting temperature in which a bulk B2/B33 interface was constructed and permitted to evolve under periodic boundary conditions in the NPT ensemble under zero total stress. A B2/B33 interface was chosen so as to minimize residual interface stress resulting from the B2/B33 lattice mismatch at this misorientation and temperature. Under

these conditions, we observed that B33 readily consumed all of the B2 in a 66 000 atom simulation cell, over timescales orders of magnitude slower than those observed during the displacive transformation, yet still readily accessible to MD simulation (see figure 4). Hence, our MD simulations suggest that the kinetics of B2/B33 interface motion would not unduly impede the B2–B33 transformation.

#### 4. Conclusions

We performed high-energy x-ray diffraction measurements of electrostatically levitated 50–50 Ni–Zr liquid droplets in which we observed that the metastable B2 phase nucleated and persisted for several seconds before the appearance of the stable B33 phase. The appearance of metastable B2 was shown to be consistent with predictions obtained from classical nucleation theory based purely on MD measurements of the driving force and SLI free energy without any fitting parameters. Further MD simulation allowed us to propose a possible scenario for the nucleation and growth of the stable B33 phase.

#### Acknowledgments

This work was supported by the US Department of Energy, Office of Basic Energy Science, Division of Materials Sciences and Engineering. The research was performed at the Ames Laboratory. Ames Laboratory is operated for the US Department of Energy by Iowa State University under Contract No. DE-AC02-07CH11358. GER's efforts were supported by the NSF under Grant DMR1308099. The authors wish

to acknowledge the assistance of K F Kelton, Mark Johnson, Chris Pueblo, Matt Blodgett, Adam Voigt, Nick Mauro and Kevin Derendorf during the BESL measurement.

## References

- [1] Notthoff C, Feuerbacher B, Franz H, Herlach D M and Holland-Moritz D 2001 *Phys. Rev. Lett.* **86** 1038–41
- [2] Ghosh G 1994 *Mater. Sci. Eng. A* **189** 277–84
- [3] Herlach D M 2001 *J. Phys.: Condens. Matter* **13** 7737–51
- [4] Li M J, Lin X, Song G S, Yang G C and Zhou Y H 1999 *Mater. Sci. Eng. A* **268** 90–6
- [5] Auer S and Frenkel D 2001 *Nature* **409** 1020–3
- [6] Auer S and Frenkel D 2002 *J. Phys.: Condens. Matter* **14** 7667–80
- [7] Shen Y C and Oxtoby D W 1996 *Phys. Rev. Lett.* **77** 3585–8
- [8] Granasy L and Pusztai T 2002 *J. Chem. Phys.* **117** 10121–4
- [9] Stranski I N and Totomanow D 1933 *Z. Phys. Chem. A* **163** 399–408
- [10] Mauro N A and Kelton K F 2011 *Rev. Sci. Instrum.* **82** 035114
- [11] Larson A C and Von Dreele R B 2004 *Technical Report* LAUR 86-748, Los Alamos National Laboratory
- [12] Bendert J C, Mauro N A and Kelton K F 2013 *J. Appl. Crystallogr.* **46** 999–1007
- [13] Kelton K F 1991 *Solid State Phys.* **45** 75–177
- [14] Mishin Y, Asta M and Li J 2010 *Acta Mater.* **58** 1117–51 [15]
- Wilson S R and Mendelev M I 2015 *Phil. Mag.* **95** 224–41 [16]
- Sun D Y, Mendelev M I, Becker C A, Kudin K, Haxhimali T, Asta M, Hoyt J J, Karma A and Srolovitz D J 2006 *Phys. Rev. B* **73** 024116
- [17] Hoyt J J, Asta M and Karma A 2001 *Phys. Rev. Lett.* **86** 5530–3
- [18] Davidchack R L and Laird B B 2003 *J. Chem. Phys.* **118** 7651–7
- [19] Aga R S, Morris J R, Hoyt J J and Mendelev M I 2006 *Phys. Rev. Lett.* **96** 245701
- [20] Turnbull D 1950 *J. Appl. Phys.* **21** 1022–8
- [21] Ragone D V 1995 *Thermodynamics of Materials* (New York: Wiley)
- [22] Hatcher N, Kontsevoi O Y and Freeman A J 2009 *Phys. Rev. B* **80** 144203
- [23] Matsuda M, Hayashi K and Nishida M 2009 *Mater. Trans.* **50** 2335–40
- [24] Asta M, Hoyt J J and Karma A 2002 *Phys. Rev. B* **66** 100101